Tropical cyclone low-level wind speed, shear, and veer: sensitivity to the boundary layer parameterization in WRF

Sara Müller[1,2], Xiaoli Guo Larsén[1], and David Verelst[1]

[1]Department of Wind Energy, Danish Technical University, Risø Lab/Campus Frederiksborgvej 399, Roskilde 4000
[2]Sino-Denmark Center (SDC) for Research and Education

Correspondence: Sara Müller (samul@dtu.dk)

Abstract. Mesoscale modeling can be used to analyze key parameters for wind turbine load assessment in a large variety of tropical cyclones. However, the modeled wind structure of tropical cyclones is known to be sensitive to the boundary layer scheme. We analyze modeled wind speed, shear, and wind veer across a wind turbine rotor plane in the eyewall and rainband region. We further assess the sensitivity of wind speed, shear, and veer to the boundary layer parameterization.

5 Three model realizations of typhoon Megi over the open ocean using three frequently used boundary layer schemes in the Weather Research and Forecasting model are analyzed. All three typhoon simulations reasonably reproduce the cyclone track and structure. The boundary layer parametrization causes up to 21 % differences in median hub height wind speed between the simulations. The simulated wind speed variability is further dependent on the boundary layer scheme. The modeled wind shear is smaller or equal to the current IEC standard regardless of the boundary layer scheme for the eyewall and rainband

10 region. While the surface inflow angle is sensitive to the boundary layer simulation, wind veer in the lowest $400\,\mathrm{m}$ of the atmospheric boundary layer is less affected by the boundary layer parametrization. Simulated wind veer reaches values up to $1.8 \times 10^{-2\,\circ}\mathrm{m}^{-1}$ ($1.1 \times 10^{-2\,\circ}\mathrm{m}^{-1}$) in the eyewall region (rainband region) and is relatively small compared to moderate wind speed regimes. On average, simulated wind speed shear and wind veer are highest in the eyewall region. Yet strong spatial organization of wind shear and veer along the rainbands may increase wind turbine loads, due to rapid coherent wind profile

15 changes at the turbine location.

1 Introduction

Research over the past decades made offshore wind power accessible for a wide region around the tropical and subtropical West Pacific. This region includes areas with large wind resources but it is frequently hit by tropical cyclones. For wind turbines in this region, tropical cyclones form the most extreme wind conditions. Therefore, the tropical cyclone wind field is a challenge

20 for wind turbine design standards. Over the past decade turbine failures have been caused during different typhoons, such as Usagi, Rammasun, and Maria (Li et al., 2022). Tropical cyclones can cause fatigue failure of a wind turbine (Chen et al., 2022). Further research incorporating mesoscale numerical models into aeroelastic wind turbine models is necessary to achieve reliable structural analysis of wind turbines in tropical cyclone conditions (Li et al., 2022).

The wind input for aeroelastic wind turbine models consists of a wind profile with an associated hub height wind speed and
wind shear over the rotor plane. In the International Electrotechnical Commission's standard (IEC), a universal constant wind
shear is suggested for load simulations (IEC, 2019). Such a simplified wind shear model has an influence on turbine loading
(Dimitrov et al., 2015). Wind veer, the change in wind direction with height is not accounted for in the IEC standards. However,
measurements from He et al. (2016) suggest that wind veer in tropical cyclones can be substantial. Similarly, Worsnop et al.
(2017) found high gust factors, rapid directional changes, and substantial veer in tropical cyclones related to non-stationary
small-scale structures in large eddy simulations. Kapoor et al. (2020) show, that these features lead to substantially increased
loads with respect to the cyclone scale mean state. Both studies highlight that wind veer should be considered in wind turbine
load assessment. Both studies from Worsnop et al. (2017) and Kapoor et al. (2020) are based on idealized Category 5 hurricane
simulation. Because of the high computational costs of large eddy simulations, mesoscale simulations remain an attractive and
important tool for assessing a large number of tropical cyclones with different intensities and storm sizes embedded in the
large-scale circulation.

However, mesoscale models are bound to parameterize sub-grid-scale turbulent transport of heat momentum and moisture
at the sea surface and in the boundary layer. The relative size of these fluxes is crucial for the intensification of tropical cy-
clones (Emanuel, 1986). It has been shown, that the choice of the boundary layer scheme affects the tropical cyclone intensity
(Gopalakrishnan et al., 2013; Rai and Pattnaik, 2018; Rajeswari et al., 2020; Zhang et al., 2020), the storm radius (Gopalakr-
ishnan et al., 2013), the boundary layer inflow strength (Gopalakrishnan et al., 2013; Rajeswari et al., 2020; Zhang et al., 2020)
and the inflow layer depth (Rai and Pattnaik, 2018; Gopalakrishnan et al., 2013; Chen, 2022). This suggests, that the tropical
cyclone mean wind speed, wind shear, and veer are sensitive to the surface and boundary layer parametrization. For moderate
wind conditions in mid-latitudes, simulated wind shear is sensitive to the boundary layer parametrization and the model per-
formance depends on atmospheric stability (Draxl et al., 2014; Krogsæter and Reuder, 2014). For tropical cyclone conditions,
the sensitivity of wind shear and veer on the boundary layer parametrization might differ from these moderate wind regimes. It
is important to know how large the associated uncertainty in these three parameters is. Because civil structures are within the
lowest hundred meters it is especially important to focus on the lower part of the boundary layer.

Mesoscale atmospheric simulations use larger grid spacing than large eddy simulations and cannot resolve sub-kilometer
scale variability (Skamarock, 2004). With that, the modeled spatial and temporal maximal values of a variable, such as wind
speed, depend on the resolved model variability (Larsén et al., 2012). Yet, extreme values are important for structural design
and load assessments, and maximal modeled wind speed is one of the most used for model verification (Rajeswari et al., 2020;
Shenoy et al., 2021). In Nolan et al. (2009) the boundary layer parametrization parameters are affected if eyewall vorticity
maxima are developed in mesoscale simulations. This suggests, that the boundary layer parametrization affects wind speed
variability in tropical cyclones.

Tropical cyclones have a characteristic wind field structure consisting of three regions. The tropical cyclone eye forms the
storm center. There, wind speeds are low and wind turbine loads are expected to be small. The wind speeds are largest and often
above wind turbine cut-out in the eyewall region. In the rainband region winds are less extreme and wind turbines might still
be operating. Wang et al. (2022) proposes a multi-stage framework to account for the difference in wind speed and turbulence

profiles between the eyewall and rainband region.

60

Accordingly, we investigate the following aspects of the tropical cyclone wind field:

1. How much is the median wind speed, shear, and veer affected by the boundary layer scheme, and how do they compare to the IEC standard?

2. What is the distribution and variability of modeled wind shear, veer, and horizontal wind speed, and how does the
65   distribution depend on the boundary layer parametrization?

3. How is wind speed, shear, and veer, spatially distributed and how does it differ between the eyewall and the rainband region?

2 Methods

2.1 Model set up

70 The open-source weather research and forecasting model (WRF) version 4.4 is used to simulate typhoon Megi, which hit Taiwan in September 2016. This case is chosen for a couple of reasons. First of all, Megi is one of the most severe storms that affected the region over Taiwan. As such it serves as a good example of severe wind conditions. Second, synthetic aperture radar data are available, in addition to the best track data sets (described in Sect. 2.3).

We run 36-hour simulations starting at 12 UTC on 25 September after a 12 h spin-up time. We compare three simulations
75 using three different boundary-layer parametrization schemes, summarized in Table 1. The goal of the study is to evaluate the spread between the best physics suits for the different boundary layer schemes. Therefore, each scheme is combined with the surface layer scheme that it has been developed with.

1. The Mellor-Yamada-Janjic boundary layer scheme (MYJ) (Janić, 2001) with the revised Eta similarity surface layer scheme (Janić, 2001).

80 2. The Mellor-Yamada-Nakanishi-Niino order 2.5 boundary layer scheme (MYNN) (Nakanishi and Niino, 2009) with the MYNN surface layer scheme (Nakanishi and Niino, 2009)

3. The Yonsei University boundary layer scheme (YSU) (Hong et al., 2006) with the revised MM5 surface layer scheme (Jiménez et al., 2012).

The YSU scheme is a first-order non-local scheme. Its eddy viscosity is described by a parabolic profile, which is itself a
85 function of boundary layer height. As a non-local scheme, YSU considers that turbulence can be regarded as surface-driven (Kepert, 2012). More precisely, in the YSU scheme, the turbulent tendencies at each vertical level are related to the heat and temperature profile throughout the boundary layer (Nolan et al., 2009). This scheme is however sensitive to the definition of the

boundary layer height (Kepert, 2012), while dynamic and thermodynamic definitions of the boundary layer height lead to different results (Zhang et al., 2011). Most studies find, that YSU performs well for tropical cyclones (Rajeswari et al., 2020). In contrast to the YSU scheme, MYJ and MYNN are local schemes. Their eddy viscosity is defined as a function of the turbulent kinetic energy, which is calculated independently at all model height levels. Many studies analyze tropical cyclones simulated with the MYJ scheme (Nolan et al., 2009; Sparks et al., 2019; Rajeswari et al., 2020; Shenoy et al., 2021), partly because it was one of only two boundary layer options in the earlier version of WRF (V2.2). The MYNN scheme is an important option for wind resource assessment in the presence of wind farm effects because wind turbine parametrizations are available for the scheme (Fitch et al., 2012; Volker et al., 2015).

The high wind speeds in tropical cyclones affect the surface fluxes. Under moderate wind conditions, the surface momentum flux over water is typically modeled using the Charnock relation (Charnock, 1955). In the Charnock relation, the drag coefficient (C_d) increases monotonically with the wind speed. As a default, the MYJ and the MYNN scheme are based on the Charnock relation and feature monotonically increasing C_d with wind speed. However, observations in Powell et al. (2003) and Donelan et al. (2004) suggest that C_d levels off for wind speeds larger than $33 \ \mathrm{ms}^{-1}$. Correcting the drag coefficient towards these findings was shown to improve modeling results (Nolan et al., 2009). In WRF version 4.4, ETA similarity surface layer scheme is the only surface layer scheme with the option to account for such a dependence of C_d on wind speed. In WRF version 4.4, it can be selected over the *isftcflx* option. We use the *isftcflx* option 2 for the YSU simulation. This option has a constant drag coefficient for wind speeds faster than $33 \ \mathrm{ms}^{-1}$ (Green and Zhang, 2013). In the default, the exchange coefficients for sensible and latent heat are a function of C_d. Using the *isftcflx* option 2, these coefficients are modified based on Garratt (1994). At $40 \ \mathrm{ms}^{-1}$ surface wind speeds, the exchange coefficients of sensible and latent heat are 40% to 50% smaller than in the default (Green and Zhang, 2013).

In all simulations, the Thompson scheme is used to parameterize the micro-physical processes (Thompson et al., 2008). On the outermost domain, convective clouds are parametrized by the Kain-Fritch (Kain, 2004) cumulus scheme. The longwave and shortwave radiation is parametrized by the RRTMG (Iacono et al., 2008) scheme. To reduce the complexity related to friction over land, we chose to focus on the cyclone intensification stage over open water, before the typhoon makes landfall. The domain setup is displayed in Fig. 1. WRF is run on three one-way nested domains, where the two innermost domains use the vortex following grid configuration. The outer domain has 350×361 grid points with a horizontal grid spacing of $18 \ \mathrm{km}$. The two inner domains have 361×361 grid points and a horizontal spacing of $6 \ \mathrm{km}$ and $2 \ \mathrm{km}$. The three domains are run with a $45 \ \mathrm{s}$ timestep on 60 vertical layers. The model top is at $200 \ \mathrm{hPa}$. For the initial and boundary conditions, ERA5 reanalysis data (Hersbach et al., 2018) is used. The sea surface temperature is used from OSTIA (Donlon et al., 2012).

2.2 Analysis method

Wind speed, wind shear, and veer are calculated from the three simulations. The analysis is based on the instantaneous model output of the innermost domain, saved every ten minutes. In the IEC, wind shear is mostly expressed as shear exponent α,

Table 1. Summary of parametrization schemes used in the three simulations.

Name	YSU	MYJ	MYNN
Boundary layer scheme	YSU	MYJ	MYNN 2.5
Surface layer scheme	MM5	Eta similarity	MYNN surface layer
Ocean surface drag	isftcflx=2	unchanged	unchanged
Micro physics scheme		Thomson et al.	
Cumulus scheme in d01		Kain-Fritsch	
Radiation physics scheme		RRTMG	
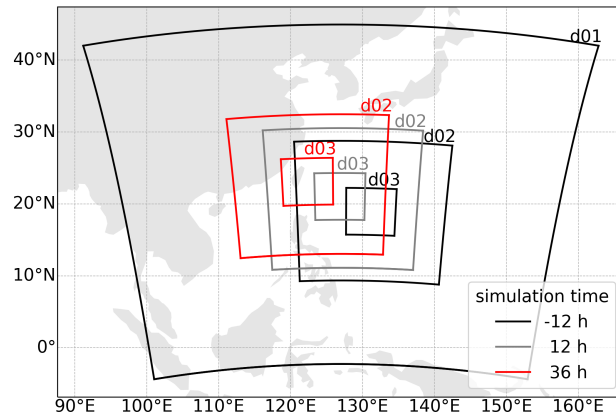
Figure 1. Domain set up: domain borders at the start of the 12 h spin-up time (black), after 12 simulation hours (grey), and after 36 simulation hours (red). Note that domain d01 is fixed in time.

which describes a power-law wind profile (IEC, 2019):

$$\frac{u_2}{u_1} = \left(\frac{z_2}{z_1}\right)^{\alpha} \tag{1}$$

Here, u_1 and u_2 are the wind speeds at heights z_1 and z_2 respectively. Wind veer is defined based on the inflow angle θ,
125 which is the angle between the tangential and the radial wind vector (Ming et al., 2022). Wind veer is then calculated from the
difference of θ between two model levels and normalized over the vertical distance between the model layers:

$$Veer = -\frac{\theta_2 - \theta_1}{z_2 - z_1}, \tag{2}$$

Here, θ is defined at the model heights z_1 and z_2. The minus sign in Eq. 2 is introduced such that positive (negative) veer
values are obtained for clockwise (counterclockwise) rotating wind vectors with height. We define z_1 and z_2 such that they
130 represent a wind turbine rotor bottom and top. For z_1 we use the height of the second model level, which has a median height
of 26 m. The seventh model level with a median height of 234 m is used as z_2. The heights are chosen as a compromise

between using model-level heights and representing a wide range of future wind turbine types planned in the Taiwan Strait based on 4Coffshore (2023). The described fictional turbine has a rotor diameter of 208 m and a hub height of 130 m. While most operating turbines in the Taiwan strait have smaller rotor diameters, 14 MW wind turbines with 222 m rotor diameter

135 are now planned in the Hailong Offshore wind farm to be operational in 2026. We further analyze the wind speed, at the fifth model level. This model level has a medium height of 139 m and is closest to the hub height of the fictional wind turbine. To understand the sensitivity of our analysis to the selection of these three heights, the profiles of wind speed and inflow angle are further analyzed. As we define shear and veer based on only two heights, only a monotonic change of wind speed and direction with height is considered. In reality, maxima might occur between the two points as found in Kapoor et al. (2020). However,

140 this is the case for only 0.3% (3.3%) of the analyzed wind speed (wind direction) profiles in our study.

The eyewall and the rainband regions are analyzed separately. These two regions are defined based on the distance to the cyclone center. The eyewall region is defined as the area with a distance to the cyclone center between 60 and 120 km. The decision of this radius range is based on the analysis of the median wind speed as a function of radius (shown in Sect. 3). It is chosen such that it includes the highest wind speeds in the simulation. The rainband region is defined as the region with a

145 distance to the cyclone center between 200 and 400 km and contains the spiraling rainbands.

Radial averages, profiles, and probability density distributions are calculated using all 144 output timesteps from the 12 UTC on 25 September to 12 UTC on 26 September. Later timesteps are not included, because of enhanced wind field asymmetries near and over Taiwan. We note, that, typhoon-land interactions are clearly important for wind turbines, and they should be addressed in future studies. All grid points within the defined radius range are used, resulting in over 120,000 points for the

150 eyewall region and 10 times more in the rainband region. The median and the interquartile range are compared between the simulations.

In this study, the cyclone track, inflow angle, and differentiation between the rainband and eyewall region are based on the definition of the cyclone center. We obtain the cyclone center with an algorithm based on the minimal variance of the sea level pressure (SLP) over bands with equal distance to the cyclone center. This center detecting method is recommended by Yang

155 et al. (2020), because it leads to a smooth track variation over time and enhanced symmetry in the wind field.

The one-dimensional power spectrum in the wave number domain is used as a measure of variability in the horizontal 10 m wind speed as in Skamarock (2004). For each time step one-dimensional spectra are calculated over the model domain for each model row (oriented approximately in the west-east direction) and column (oriented approximately in the north-south direction). Before calculating the spectra, linear trends in the rows and columns are removed by individually subtracting the

160 result of a linear least-squares fit. The spectrum is obtained by Fourier transform. Ten grid points at the grid edges are removed to avoid the sponge-layer effects related to the domain nesting. This results in 2×341 spectra per time step. These spectra are averaged over all 144-time steps between 12 UTC on 25 September and 12 UTC on 26 September.

2.3 Validation method

The model data is compared to and qualitatively validated against the best track data. Best track data is publicly available

165 from different meteorological centers. In this study best track data sets from two centers are used: the US Joint Typhoon

Warning Center (JTWC) and the Regional Specialized Meteorological Center (RSMC) Tokyo-Typhoon Center operated by the Japan Meteorological Agency (JMA). Both data sets include the cyclone's central position in three to six-hour intervals. The best track data sets further include the central pressure and the maximal sustained wind speed. These are mainly based on the method described by Dvorak (1984) (RSMC, 2021; Chu et al., 2002). The maximal sustained wind speed is defined

170   differently in the two data sets. JTWC reports the maximal one-minute sustained wind speed (Chu et al., 2002), defined as the maximal 10 m wind speed averaged over 1 minute encountered over the entire cyclone structure. JMA in contrast reports the maximal ten-minute sustained wind speed, giving the maximal 10 minute average wind speed (RSMC, 2021). The conversion between the two metrics is not straightforward. Harper et al. (2010) recommends a conversion factor of 0.93 between the larger one-minute sustained wind speed and the ten-minute sustained wind speed over the ocean. Chu et al. (2002) states that the

175   one-minute sustained wind speed is in general around 14% larger than the ten-minute sustained wind speed. This results in a conversion factor of 0.88, and a larger difference between the two data sets. The difference between the sustained wind speed in the two data sets is even larger than 14% (Ott, 2006). We decided to use both best track data sets to see the model spread in relation to the spread in the best track data. For easier comparison, we additionally provide the JTWC one-minute sustained wind speeds converted to ten-minute sustained wind speeds. We use, the factor 0.93 recommended by Harper et al. (2010) for

180   the conversion.

We further use Synthetic Aperture Radar (SAR) wind scenes for the validation of the modeled horizontal wind speed structure and variability. Wind scenes are post-processed by Badger et al. (2022) and taken from the European space agency (ESA). This study uses eight wind scenes, that cover different areas of typhoon Megi between 9 and 22 UTC on 26 September 2016. The scenes are shown in Fig. 2. The scenes provide the 10 m wind speed in a regular 500 m grid. One-dimensional power spec-

185   tra are calculated from the eight wind scenes in the same way as for the model data (see Sect. 2.2). The spectra are calculated over the axis with the larger number of grid points and averaged over the shorter axis for each of the eight SAR wind scenes.

Lastly, the wind profile structure is compared to global positioning system dropsonde measurements documented in Powell et al. (2003) and Vickery et al. (2009). The measurements include 331 profiles from 15 tropical cyclones over the Atlantic Eastern and Central Pacific. Based on these measurements Vickery et al. (2009) suggests an empirical formulation for the

190   tropical cyclone boundary layer which accounts for a low-level jet:

$$U(z) = u_*/\kappa[ln(z/z_0) - a(z/H^*)^n], \tag{3}$$

Here, u_* is the friction velocity, κ the von Kármán coefficient, z the height, z_0 the surface roughness length, and H^* a boundary layer height parameter. The parameters a and n are free parameters fitted to the dropsonde measurements. Vickery et al. (2009) analyze the dropsonde measurements in a composites sense. They group the measurements according to the radius of maximal

195   winds (RMW) and the mean boundary layer (MBL) wind speed. The latter is defined as the mean wind speed over a height range of 10 to $500\,\mathrm{m}$. Based on the JTWC best track dataset, typhoon Megi's RMW is mostly in the range of 30-60 km during the analyzed period. The MBL wind speed is calculated from the simulated eyewall profiles. Depending on the boundary layer scheme used in the simulation, the MBL wind speed is in the range of 30-39 $\mathrm{m\,s^{-1}}$ or 40-49 $\mathrm{m\,s^{-1}}$. With that, we can compare the simulated wind profiles with two wind profiles defined by parameter-sets given by Vickery et al. (2009), describing wind
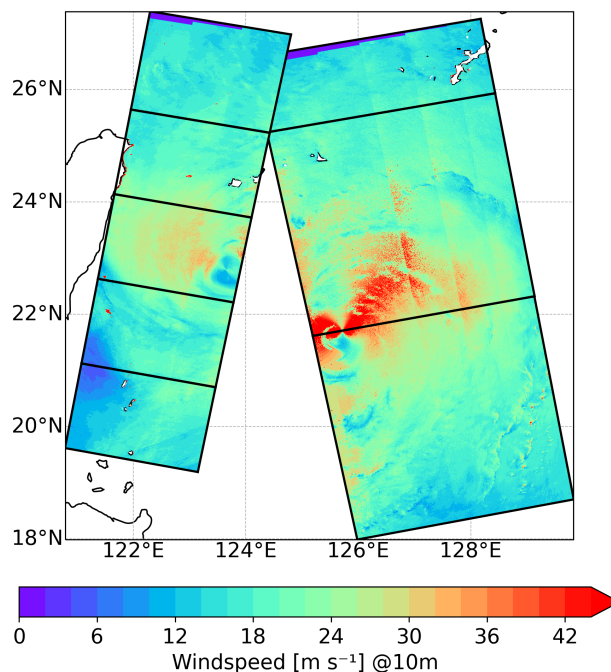
Figure 2. Synthetic aperture radar wind scenes used for model validation. The five wind scenes on the western side are taken between 9.35 and 9.38 UTC and the three on the eastern side between 21.31 and 21.46 UTC on 26 September 2016. The wind scenes are retrieved from Badger et al. (2022).

profiles with the corresponding RMW and the two MBL wind speed ranges. Vickery et al. (2009) further assess two methods to obtain the parameter-sets for each group. Both parameter-sets are used in our study. To compare the vertical wind shear from the dropsonde measurements to the analyzed simulations, α is calculated from Eq. 1.

3 Results

3.1 Model verification against best track data

Cyclone Megi develops from a tropical disturbance in the western Pacific Ocean and reaches tropical cyclone intensity on 24 September. Megi's track and intensity in terms of minimal SLP and maximal wind speed from 25 September onward are shown in Fig. 3. On 24 September cyclone Megi continues its trajectory north-westwards toward Taiwan. During this trajectory over the open ocean, Megi intensifies. Its minimal SLP decreases and the maximal wind speed increases and reaches a maximum at 00 UTC on 27 September (see Fig. 4). On 27 September Megi hits Taiwan and weakens. This can be seen in the consequent increase of the minimal SLP and the decrease in wind speed. After entering the Taiwan strait Megi makes landfall over mainland China between 18 UTC on 27 September and 00 UTC on 28 September.
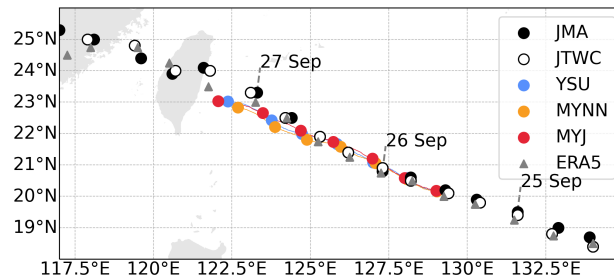
Figure 3. Typhoon track: Cyclone center position of the YSU (blue), MYNN (red), MYNN-eta (purple), and MYJ (yellow) simulation and of the best track data sets JMA (black filled points) and JTWC (white filled points). Points show the position at 00, 06, 12, and 18 UTC. Lines show the position every 10 minutes for the simulations.

The simulations cover the period between 12 UTC on 25 to 00 UTC on 27 September when Megi intensifies over the open ocean. During this time, the two best track data sets are in close agreement in terms of central position (Fig. 3). All three simulations can reproduce the general cyclone track, with only a slight southward deflection. The error at the end of the simulations is within 130 km. The error in the simulated track is larger than in the ERA5 dataset, which is used as boundary conditions. The simulations can further reproduce cyclone intensification (Fig. 4). However, the degree of intensification varies between the simulations. From Fig. 4 it can be seen that the minimal SLP drops initially at the highest rate in the MYJ simulation. However, at 6 UTC on 26 September, the MYJ simulation stops intensifying. At the simulation end, the minimal SLP of the MYJ and the YSU schemes are similar. The minimal SLP of both MYJ and YSU is mostly between the minimal SLP from the JTWC and the JMA best track data set. The difference in the simulated minimal SLP between these two simulations is smaller than between the best track datasets. Similarly, the maximal wind speed of the YSU and the MYJ simulation is between the maximal ten-minute sustained wind speed reported by JMA and the maximal one-minute sustained wind speed reported by JTWC. Differently, the typhoon in the MYNN simulation intensifies less than in the JMA and JTWC best track data sets. Its minimal SLP follows the higher minimal SLP of the coarser ERA5 data. The MYNN maximal wind speed follows the maximal ten-minute sustained wind speed reported by JMA and is lower than in the YSU and MYJ simulations.

3.2 Mean wind field

We analyze the characteristic structure of a tropical cyclone through an example simulation timestep at 00 UTC on 26 September. This timestep is the center of the analyzed period from 12 UTC on 25 September to 12 UTC on 26 September. The horizontal wind field at $10\,\mathrm{m}$ at that time is given in Fig. 5 a-c for the three different boundary layer schemes. In the eye, the center of the storm, wind speeds are near zero. Outside of the eye, the wind rotates in a circular pattern counterclockwise. Larger wind speeds are evident in the top right quadrant, northwestward of the eye. Nevertheless, the symmetric wind speed component dominates over asymmetric features. This allows averaging the wind field over the azimuth, as shown in Fig. 6. Based on the averaged wind over time and azimuth, we can systematically compare the wind speed in the three simulations.
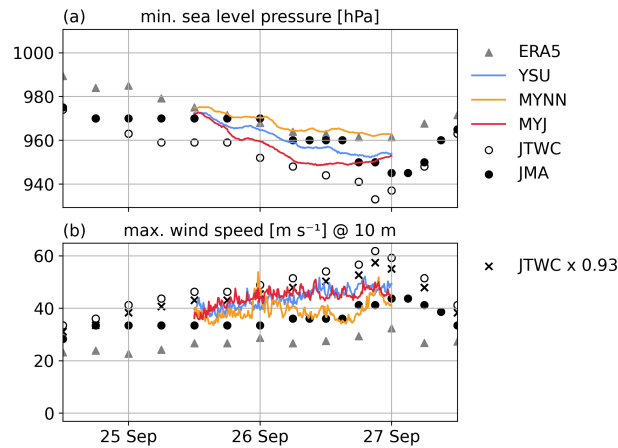
Figure 4. Cyclone intensity in terms of a) minimal SLP of the simulations (lines) and the ERA5 reanalysis data (triangles) compared to the best track data (circles) and b) maximal instantaneous wind speed in the simulations (lines), the ERA5 reanalysis (triangles), the maximal ten-minutes sustained wind field from JMA (black points), and the maximal one-minute sustained wind field from JTWC (white points). Black crosses show the JTWC values multiplied by 0.93, as recommended by (Harper et al., 2010) to convert ten-minute sustained wind speeds to one-minute sustained wind speeds in tropical cyclones over the sea.

Wind speeds are maximal in the eyewall. There, the 10 m wind speeds are in the median $32\mathrm{m\,s^{-1}}$ in the YSU and the MYJ
235 simulations. The MYNN simulation shows a $12\mathrm{m^{-1}}$ lower 10 m eyewall wind speed than the MYJ and the YSU simulation. This qualitatively agrees with the lower maximal wind speed in the MYNN simulation over the entire simulation period as described in Sect. 3.1. Additionally, the distance between the eye and eyewall is larger in the MYNN simulation than in the YSU and the MYJ simulations. In terms of the radius of maximal averaged wind, the difference is 12 km (10 km) with respect to the YSU (MYJ) simulation. With increasing distance from the eyewall outwards, the wind speed gradually decreases. The
240 radial gradient in wind speed is most pronounced in the MYJ simulation. In the eyewall region, the surface wind speeds are highest in the YSU simulation, followed by the MYJ simulation and the MYNN simulation.

The simulated vertical wind field structure is analyzed based on profiles of wind speed and inflow angle. The wind speed increases with height as shown in Fig. 7. The structure of the simulated profiles qualitatively agrees with the structure of dropsonde measurements reported by Vickery et al. (2009). The simulated profiles are characterized by a jet at around 800 m
245 in the eyewall region and at 1200 m in the outer cyclone. Below the jet, the simulations have an approximately logarithmic wind speed increase with height. The simulated wind profiles differ in two aspects: Firstly, the wind shear below the jet nose is more pronounced in the YSU simulation with respect to the profiles from Vickery et al. (2009) and the MYNN and MYJ simulation. Secondly, the slope of the logarithmic wind profile is larger in the MYJ simulation, than in the profiles from Vickery et al. (2009), the MYNN simulation and particularly in the YSU simulation. The change in wind speed with height is given in
250 terms of α in Fig. 8 and Table 2. The simulated median α ranges from 8.6×10^{-2} to 1.1×10^{-1} in the eyewall. This is in good agreement with the α-values obtained from the profiles form Vickery et al. (2009), which are within 9.1×10^{-2} and 9.6×10^{-2}
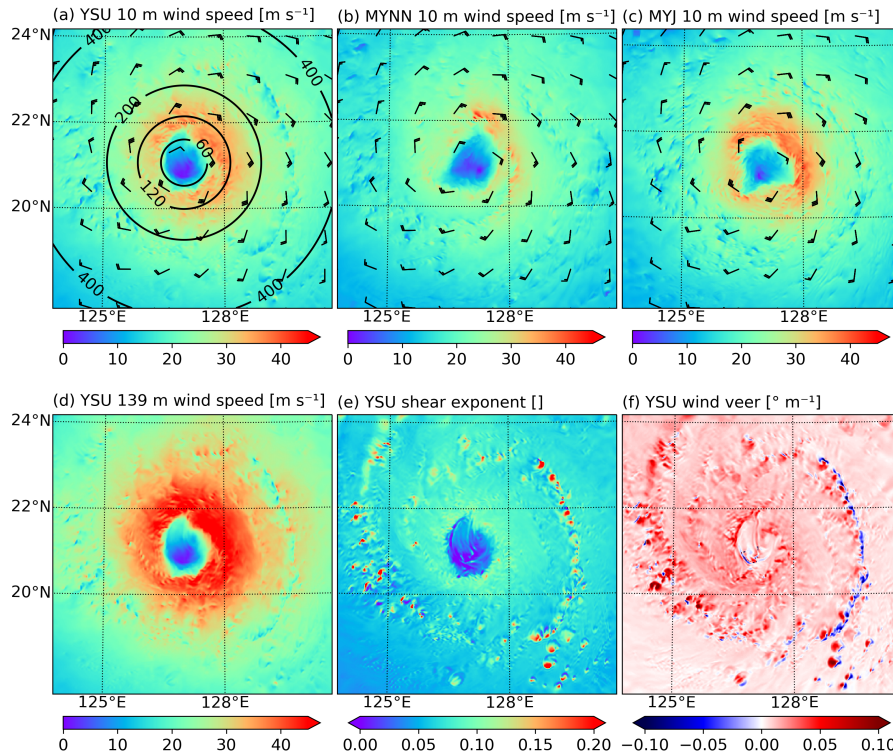
Figure 5. Horizontal fields taken from the model output at 12 UTC on 26 September. a-c) show the instantaneous horizontal wind field at 10 m in the YSU, MYNN, and MYJ simulation. d-f) show the YSU d) wind speed at 139 m, e) wind shear defined as bulk wind speed difference between 234 and 26 m, and f) wind veer defined as the difference in the inflow angle between 234 and 26 m. Black contours in a) mark circles of 60, 120, and 400 km distances from the cyclone center.

for the selected profiles. Compared to the eyewall region, the simulated α-values are smaller in the raindband region, where they are in the range of 6.6×10^{-2} to 9.6×10^{-2}. The larger slope in the MYJ simulation with respect to the YSU reflects in 2.4×10^{-2} (3.0×10^{-2}) larger shear exponent in the exponent in the eyewall (rainband) region.

255 The difference in the slope of the wind profile is important for wind turbines because it controls the wind at hub height and the wind shear over the rotor plane. At hub height, the horizontal wind speed has an analog structure as the surface wind field but an increased magnitude (Fig. 5 d). With the larger gradient in wind speed with height, the MYJ simulation has a $1.9 \, \mathrm{m \, s^{-1}}$ larger eyewall wind speed at hub height than the YSU scheme, while having a similar wind speed at 10 m (see Fig. 8 and Table 2). At hub height, the MYNN simulation has $7.9 \, \mathrm{m \, s^{-1}}$ ($6.0 \, \mathrm{m \, s^{-1}}$) smaller wind speed than MYJ (YSU). The

260 wind speed in the rainbands at hub height is similar in the MYJ and the YSU and smaller in the MYNN simulation.

 The inflow angle is shown as a function of height in Fig. 7. All schemes exhibit a median inflow with a depth of around $1000 \, \mathrm{m}$. The surface inflow angle is clearly smaller in the MYNN simulation than in the YSU and the MYJ simulation. Within the inflow layer, the mean wind turns outward with respect to the cyclone center with height. The change in the inflow angle
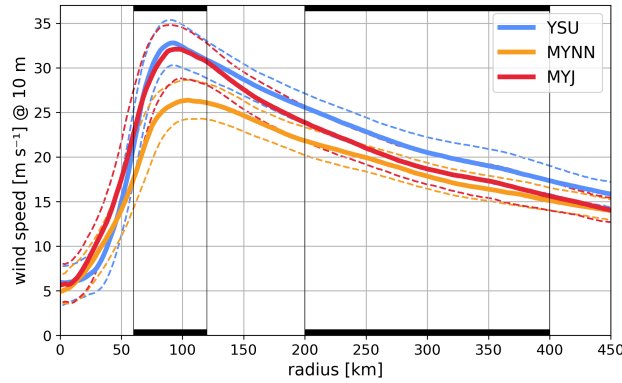
Figure 6. 10 m wind speed as a function of distance from the cyclone center for the YSU, MYNN, and MYJ simulation: median (solid line) and 0.25 and 0.75 percentiles (dashed lines). Black bars mark the eyewall region (60-120 km) and the rainband region (200-400 km). The values are obtained from all grid points within 144 output time-steps between 12 UTC on 25 September and 12 UTC on 26 September, analyzed in bins of 2 km radius.

Table 2. Median and interquartile range (IQR) of wind speed at 139 m, wind shear, and wind veer for the eyewall region (60-120 km distance to cyclone center) and rainband region (200-400 km distance to cyclone center) for the YSU, MYJ, and MYNN simulation.

Parameter	Scheme	R [km] $\in [60, 120]$		R [km] $\in [200, 400]$	
		median	IQR	median	IQR
	YSU	39.8	8.1	25.1	6.0
wind speed [m s^{-1}]	MYNN	33.8	7.5	23.4	5.6
	MYJ	41.7	9.8	24.6	6.3
	YSU	8.6×10^{-2}	1.7×10^{-2}	6.6×10^{-2}	1.8×10^{-2}
Shear exponent []	MYNN	9.5×10^{-2}	1.9×10^{-2}	9.0×10^{-2}	2.0×10^{-2}
	MYJ	1.1×10^{-1}	1.7×10^{-2}	9.6×10^{-2}	2.0×10^{-2}
	YSU	1.7×10^{-2}	9.7×10^{-3}	8.1×10^{-3}	7.8×10^{-3}
Wind veer [$^\circ$ m^{-1}]	MYNN	1.8×10^{-2}	9.0×10^{-3}	1.1×10^{-2}	7.4×10^{-3}
	MYJ	1.8×10^{-2}	9.6×10^{-3}	1.1×10^{-2}	7.9×10^{-3}

with height is relatively constant in the lowest $400\,\text{m}$ of the boundary layer and comparable between the three simulations.
265 The resulting wind veer is in close agreement between the three simulations. The simulated median wind veer ranges from $-1.7 \times 10^{-2\,\circ}\,\text{m}^{-1}$ to $-1.8 \times 10^{-2\,\circ}\,\text{m}^{-1}$ in the eyewall region and from $-8.1 \times 10^{-3\,\circ}\,\text{m}^{-1}$ to $1.1 \times 10^{-3\,\circ}\,\text{m}^{-1}$ in the rainband region (see Fig. 8 and Table 2).
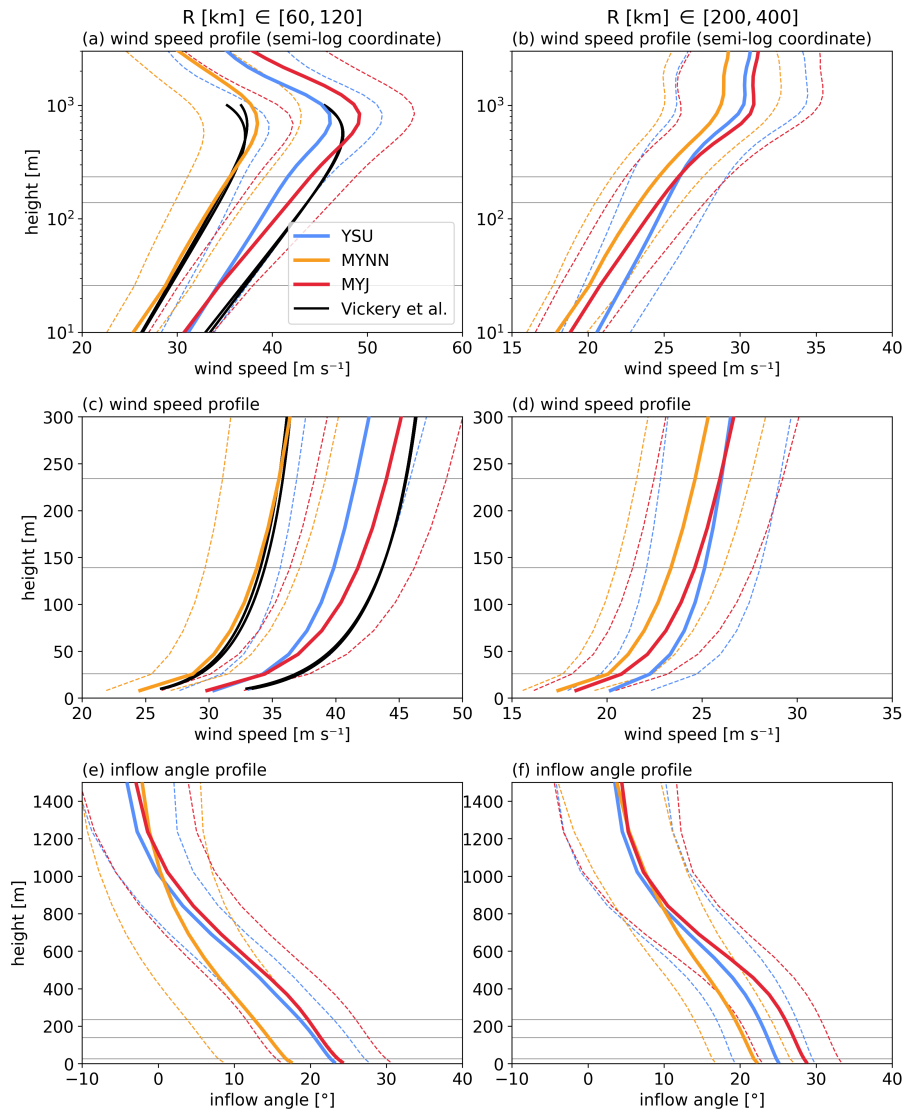
Figure 7. a-d) wind speed profiles and e-f) inflow angle profiles in a,c,e) the eyewall region (60-120 km distance to cyclone center) and b,d,e) the rainband region (200-400 km distance to cyclone center). a-b) use semi-locarithmic coordinates in order to emphasize the logarithmic structure of the wind profile. Solid lines show the median and dashed lines show the 0.25 and 0.75 percentiles. Horizontal lines show the heights of 26, 139, and 234 m. The values are obtained from all grid columns within the defined radius bands in 144 output time-steps, between 12 UTC on 25 September and 12 UTC on 26 September.

3.3 Wind variability

Apart from the large-scale structure, the simulations also produce variability in the wind field. Finer-scale wind fluctuations

270   can be seen in all simulations within and outside of the eyewall in Fig. 5. To compare the variability of wind speed between
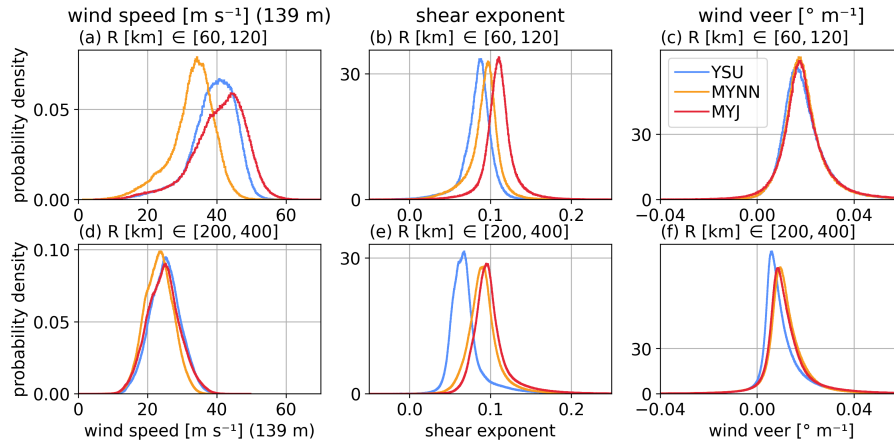
Figure 8. Probability density of wind speed at $139\,\mathrm{m}$, wind shear exponent, and wind veer for the eyewall region (60-120 km distance to cyclone center) and the rainband region (200-400 km distance to cyclone center) for the YSU, MYJ, and MYNN simulation.
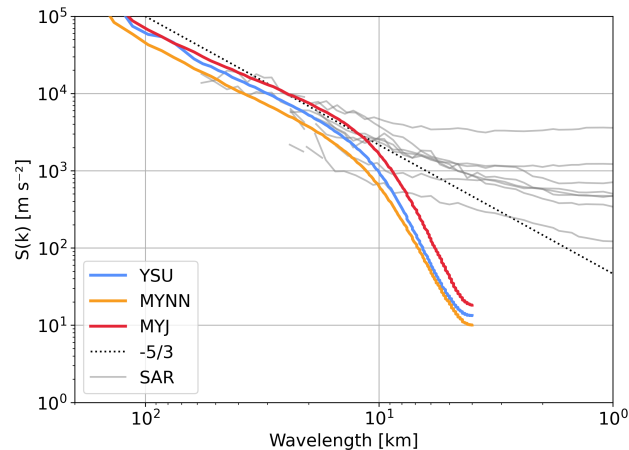
Figure 9. One-dimensional power spectrum in the wave number domain for the three simulations (color) and eight SAR wind scenes (grey). The slope of minus five-thirds is shown for reference (dashed). For better readability, logarithmic averaging is applied to the spectra.

the simulations, the one-dimensional wind speed power spectra in the wave number domain is analyzed in Fig. 9. In agreement with the wider wind speed distribution, MYJ shows the highest power spectral density over the calculated wavelength range of 6 to $300\,\mathrm{km}$ and MYNN the lowest. The spectra can be divided into two parts:

1. For wavelengths larger than $15\,\mathrm{km}$, the YSU and MYNN simulated spectra have a slope of approximately minus five-thirds and a slightly smaller slope for MYJ. The smaller slope in the MYJ simulation particularly increases the spectral power density contribution from higher wave numbers. The MYJ slope in this range fits the mean spectral slope obtained from the SAR images the best. Also, the magnitude shows the best fit for the MYJ simulation.

275

2. For wavelengths smaller than $15\,\mathrm{km}$ the simulated spectra have a smaller slope than minus five-thirds. Differently, the spectra from the SAR images have larger slopes than minus five-thirds. In other words, the energy level of the simulations drops stronger with increasing wave number than observed. This shows, that the spectral tails are damped in the simulations consistent with Skamarock (2004) and Larsén et al. (2012).

For the scenes analyzed, namely, before being affected significantly by land, the IQR of wind veer and wind shear are nearly insensitive to the boundary layer scheme. In all simulations, the spatial distribution of shear and veer is not uniform. In the rainband region, the maximal values of shear and veer are found along the spiraling rainbands (Fig. 5). Along the rainbands, there is a zone of lower horizontal wind speed. Within this zone, local maxima and minima of wind shear are alternating. The wind veer changes from negative values (inflow angle decreasing with height) on the radially inward side of the rainbands to positive values (inflow angle increasing with height) on the outside.

4 Discussion

The three WRF simulations using the MYNN, YSU, and MYJ boundary layer schemes are able to produce a typhoon with a physically realistic track in terms of propagation speed and direction. Track position discrepancies are within $130\,\mathrm{km}$. As the track of the ERA5 reanalysis data shows good agreement with the best track data sets, it is evident that the track errors develop within the simulations. The higher SLP at the end of the MYNN simulation indicates, that this simulation underestimates Megi's intensity. However, this doesn't directly lead to the conclusion that the MYNN boundary layer scheme produces overly weak cyclones in general. On one hand, the best track datasets are mainly based on satellite observation, without direct in-situ measurements. This leads to uncertainty in the data as reflected by the spread of the JMA and JTWC data sets. On the other hand, the results of this study cannot readily be generalized to tropical cyclones with different intensities and storm sizes. At last, accounting for atmosphere ocean, and atmosphere wave interactions may further improve model performance and simulated tropical cyclone intensity.

Given that many factors play into the model results, one may question how representative the selected case is. We argue that the differences between the MYNN simulation on the one hand and the YSU and MYJ simulation on the other hand strongly agree with documented sensitivity studies. Similar to our case, Rajeswari et al. (2020) found weaker storms for MYNN than for YSU, and most intense storms for MYJ, related to weaker low-level inflow in the MYNN scheme for five cyclones over the Bay of Bengal using WRF version 3.8. MYNN's lower intensity most likely relates to higher vertical diffusion in the MYNN scheme, which has been found to result in less intense storms, larger radius of maximal wind speed, and weaker radial inflow (Kepert, 2012; Gopalakrishnan et al., 2013; Zhang et al., 2020). The differences in the radius of maximal wind speed between the three simulations (see Fig. 6) most likely relate to the cyclone intensity and eddy-viscosity (Gopalakrishnan et al., 2013; Zhang et al., 2020).

For extreme wind conditions, the IEC standard proposes to use a α of 1.1×10^{-2} (IEC, 2019). The simulated α is in the median equal to or less than the IEC standard for all boundary layer schemes. This suggests, that the shear for extreme wind defined in the IEC standard is as steep or steeper when compared to typhoon Megi before landfall. This conclusion is in

agreement with the α-values obtained from Vickery et al. (2009). The mean shear profiles from LES simulations in Kapoor et al. (2020) have even smaller α-values, than those obtained in our study. This supports the conclusion, that the current IEC standard is sufficiently similar in terms of wind shear during tropical cyclones. The simulated α are similar in their order of magnitude and in their sensitivity to the boundary layer scheme to simulations during neutral atmospheric stability at an

315   offshore location in Denmark Krogsæter and Reuder (2014). In neutral atmospheric stability Krogsæter and Reuder (2014) find that the YSU scheme produces simulation with smaller α (7.7×10^{-2}) compared to the MYNN (8.8×10^{-2}) and the MYJ (1.09×10^{-2}) simulation similar to the results of our study.

In contrast to our simulations over the open ocean, He et al. (2016) and Tse et al. (2013) use wind observations in coastal areas. Both studies find wind shear larger than in the current IEC standard during typhoon conditions. He et al. (2016) find α

320   in the range of 0.152 to 0.175 for profiles with marine exposures during 22 typhoons over Hong Kong. Tse et al. (2013) find α-values of 0.14 to 0.25 during typhoon Fengshen and Molave for profiles with marine exposure. The larger wind shear in these two studies could be a suggestion that wind shear may increase during the landfall of a tropical cyclone. Further studies are needed to understand how wind shear and veer evolve during landfall.

The simulated wind veer is relatively small in comparison to wind veer found in low-wind regimes and particularly in stable

325   conditions. This result stands in contrast to Kapoor et al. (2020) and He et al. (2016) who find significant wind veer in LES simulations and observations respectively. The maximal 10-minute wind veer from during tropical cyclone conditions from LES simulations in Kapoor et al. (2020) is in the order of $1.4 \times 10^{-1}\,^{\circ}\,\mathrm{m}^{-1}$ over the rotor diameter and with that around eight times larger than in the median values and three times larger than the 99 percentile in our simulations. The differences between the study from Kapoor et al. (2020) and the simulated wind veer in our simulations can come from higher resolved wind veer

330   variability in LES simulations or an overall shifted wind veer distribution. He et al. (2016) finds wind veer in the order of $2.8 \times 10^{-2}\,^{\circ}\,\mathrm{m}^{-1}$ from the surface to the height of maximal wind speed from wind direction measurements with an open water fetch over a coastal area. This is around $0.003^{\circ}\,\mathrm{m}^{-1}$ larger than the wind shear in the YSU and MYJ simulation between the surface and $800\,\mathrm{m}$ (the height of simulated maximal wind speed) and around $0.01\,^{\circ}\,\mathrm{m}^{-1}$ larger than in the MYNN simulation. Similar to the larger wind shear in the study from He et al. (2016), the difference between the studies may originate from the

335   different locations with respect to land.

The simulated profile structure qualitatively agrees with the structure of dropsonde measurements from Vickery et al. (2009). However, the structure of the jet nose in the YSU simulation differs from their engineering model (Eq. 3). The engineering model describes a decreasing slope in a semi-log plot with height. Differently, the profiles of the YSU simulation have an increase in their slope below the height of the jet. This can be seen in Fig. 7 between $250\,\mathrm{m}$ to $800\,\mathrm{m}$ ($300\,\mathrm{m}$ to $1000\,\mathrm{m}$) in the

340   eyewall (rainband) region. However, it is not given that the empirical formulation holds for typhoon Megi because the MBL wind speed in the YSU simulation is larger than $40\,\mathrm{m\,s}^{-1}$. For such high wind speed profiles, an increase in slope with height below the jet nose is detectable in Fig. 2 and 8 in Vickery et al. (2009). Likewise, He et al. (2022) observed that the curvature of the typhoon wind profile is larger than predicted by the logarithmic law at heights of around $200\,\mathrm{m}$. However, they suggest that this relates to an internal boundary layer forming over land. This enhanced vertical wind speed gradient in the YSU simulation

345   is located at heights not relevant for current wind turbines. More relevant for the analysis of shear is a small derivation from

the logarithmic wind profile in the MYNN simulation. The slope of the semi-log wind profile is higher between the first and the second model layer than above. The difference is only slightly detectable in Fig. 7a) at $26\,\mathrm{m}$. This change in slope was more pronounced in model runs with larger vertical grid spacing (not shown). The change in wind shear makes the analysis of wind shear using Eq. 1 sensitive to the selection of the heights z_1 and z_2 and to the vertical model resolution. The same

350   analysis with a coarser vertical grid spacing, using the first instead of the second model level for z_1, resulted in increased wind shear values for the MYNN simulation (not shown). However, from the second model level upwards to $250\,\mathrm{m}$ all simulations closely follow a logarithmic wind profile and have a constant change in inflow angle with height. The qualitative differences in modeled shear and veer are therefore consistent for model heights above the second model level. For completeness, we report on finding discontinuous profiles with the MYJ boundary layer scheme in simulations with more vertical model levels (WRF

355   version 3.7.1, fixed domains, 80 vertical layers). The discontinuities were found between 40 and 300 m and appeared to be related to the fine vertical grid spacing. This gave an incentive to lower the number of vertical levels in the current study.

The maximal 10 m wind speed of the simulations lies within the given values of the two best track data sets. This shows that the maximum of the 10 m wind speed from a $2\,\mathrm{km}$ grid is a valid approximation for the maximal ten-minutes sustained

360   wind field. In contrast, the maximal wind speed in the ERA 5 reanalysis has clearly lower maximal wind speeds. Following Nolan et al. (2009), a relative agreement between the simulated maximal wind speed and the then-minute sustained wind field in the studied simulations is expected as explained subsequently. As seen in Fig. 9, the horizontal variability can be reproduced to scales of around $X = 15$ km. The fastest simulated wind speeds at $10\,\mathrm{m}$ are in the order of $WS = 40\ \mathrm{m\,s^{-1}}$ (see Fig. 6). The associated resolved simulated temporal resolution corresponds to $X/WS \simeq 6$ minutes. The effective spatial resolution of

365   approximately 15 km corresponds to $7.5 \times$ the horizontal grid spacing (2 km in our simulations) in agreement with Skamarock (2004). The loss of variability on scales smaller than 15 km is related to horizontal diffusion in WRF (Skamarock, 2004).

The spectral slope of minus five-thirds found for both simulations and SAR data for wavelength larger than 15 km, agrees with Gage and Nastrom (1986). At smaller wavelengths, the spectral energy density in the SAR products increases with decreasing wavelength. This can be attributed to the superposition of three-dimensional turbulence on top of the mesoscale

370   quasi-two-dimensional turbulence (Karagali et al., 2013; Larsén et al., 2016). The mean magnitude of the SAR spectra agrees best with the MYJ spectra for wavelengths larger than 15 km. However, the magnitude of the SAR spectra depends on what typhoon area is covered in the SAR image and of the analysed time step. Because the area differs from the area covered by the simulation domain, comparing their magnitude provides only limited insight. Furthermore, the mean wind speed obtained by the SAR product might be subject to uncertainty, as SAR calibration over extreme wind areas is rare. In fact, SAR products with

375   significantly higher wind speeds are given by Jackson et al. (2021). These were in good agreement with the JTWC best track data, as opposed to the here-used SAR product being closer to the JMA data set, which of course depends on the algorithms for the specific SAR retrievals for their case.

5 Conclusions

Due to the potentially large influence on wind turbine loads, we analyze hub height wind speed, wind shear, and wind veer
380 over the rotor plane. The horizontal distribution and variability of these parameters are analyzed in the eyewall and rainband
region of typhoon Megi (2016) using a mesoscale modeling framework. To evaluate model uncertainty related to the boundary
layer parametrization, three frequently used boundary layer schemes (MYJ, MYNN, and YSU) are analyzed in WRF(V4.4).

Our analysis showed that:

1. All three simulations can reasonably reproduce the typhoon track and cyclone structure. The storm intensifies in all
385   model realizations and the spread of the simulated storm intensity is comparable to the spread between best track data
   sets. With that, the spread between the models in wind speed, wind shear, wind veer and their variability can be regarded
   as model uncertainty.

2. Simulated hub height wind speed is sensitive to the boundary layer parametrization and its median varies between the
   schemes by 21% (7%) in the eyewall (rainband) region.

390 3. Regardless of the boundary layer parametrization the simulated median wind shear exponents (α) is smaller or equal to
   0.11 suggested in the IEC standards (IEC, 2019). The simulated wind shear is in good agreement with the study from
   Vickery et al. (2009), but clearly smaller than observed in coastal areas during tropical cyclone conditions (Tse et al.,
   2013; He et al., 2016). The difference in the median α between the simulations using different boundary layer schemes
   is 2.4×10^{-2} (3.0×10^{-2}) in the eyewall region (rainband region). This difference is small compared to the difference
395   between the simulated offshore typhoon and observations over coastal areas (Tse et al., 2013; He et al., 2016).

4. Median wind veer is up to $1.8 \times 10^{-2\,\circ}\,\mathrm{m}^{-1}$ ($1.1 \times 10^{-2\,\circ}\,\mathrm{m}^{-1}$) in the eyewall (rainband) region and nearly constant in
   the lowest $400\,\mathrm{m}$ of the boundary layer. The simulated wind veer is relatively small compared to wind veer in moderate
   wind speed regimes. This stands in contrast to studies from Worsnop et al. (2017), Kapoor et al. (2020) and He et al.
   (2016) who found strong wind veer in tropical cyclone simulations. The difference in wind veer between the different
400   simulations is $1.0 \times 10^{-3\,\circ}\,\mathrm{m}^{-1}$ ($2.9 \times 10^{-3\,\circ}\,\mathrm{m}^{-1}$) in the eyewall (rainband) region and small relative to the wind veer
   found in He et al. (2016), Worsnop et al. (2017) and Kapoor et al. (2020).

5. Spectral analysis of the three simulations with a $2\,\mathrm{km}$ horizontal grid spacing shows, that horizontal wind speed variabil-
   ity is resolved on scales larger than $15\,\mathrm{km}$ as expected. The variability is largest in the MYJ simulation followed by the
   YSU simulation and smallest in the MYNN simulation. The produced horizontal difference in variability between the
405   three schemes is evident over the analyzed wavelength range (4-100 km). Because the spectral energy density decays less
   with increasing wavenumber in the MYJ scheme, the difference in horizontal wind speed variability is most pronounced
   at the smallest resolved wavelengths.

6. The distribution of shear and veer are nearly insensitive to the boundary layer schemes and the interquartile range varies
   up to 11% between the schemes.

7. Overall hub hight wind speed, wind shear, and wind veer are larger in the eyewall region than in the rainband region. Within the rainband region, a clear spatial organization of wind shear and veer is found along the spiraling rainbands. In fact, local maxima in shear and veer along the rainbands are larger than the maximal simulated values in the eyewall region. On the radially inward side of the rainbands, positive veering angles reach their maximum over the tropical cyclone structure. On the outward either small wind veering angles or backing (negative wind veer) dominate. Wind shear maxima and minima on scales of around 20 km alternate along the rainband. This spatial organization likely leads to rapid coherent changes in the wind profile at a possible wind turbine location.

Based on these conclusions we suggest further investigating, 1.) how wind speed, shear, and veer in tropical cyclones evolve during landfall, 2.) how much wind shear and wind veer vary between tropical cyclones with different intensities and radii, and 3.) how much wind turbine load estimates based on the current IEC standard differ between load estimates based on the simulated wind speed, shear, and veer distributions.

Code and data availability. The source code of the WRF model is available at https://www.mmm.ucar.edu/models/wrf (Skamarock et al., 2021). The ERA 5 data used as boundary conditions for the WRF simulation is available at https://doi.org/10.24381/cds.bd0915c6 (Hersbach et al., 2018). The JTWC best track dataset is available at https://www.metoc.navy.mil/jtwc/jtwc.html?best-tracks (Chu et al., 2002) and the JMA best track dataset is available from https://www.jma.go.jp/jma/jma-eng/jma-center/rsmc-hp-pub-eg/trackarchives.html. The SAR data is available at https://doi.org/10.11583/DTU.19704883.v1 (Badger et al., 2022).

Author contributions. SM, XGL planned the study; SM performed the model simulations with input from XGL; SM conducted the model analysis with input from XGL and DV. SM wrote the manuscript draft; XGL, DV reviewed and edited the manuscript.

Competing interests. The authors declare that no competing interests are present.

Acknowledgements. This study is supported by the SDC project 906421. The authors acknowledge the computational and data resources provided on the Sophia HPC Cluster at the Technical University of Denmark (DTU), DOI: 10.57940/FAFC-6M81. We thank Jana Fischereit and Ebba Dellwik from DTU for the feedback on the paper draft. We further thank Marc Imberger and Oscar Manuel Garcia Santiago from DTU for their help and discussions.

References

4Coffshore: Global Offshore Wind Farms, available at http://www.4coffshore.com, last accessed 25 May, 2023.

435   Badger, M., Karagali, I., and Cavar, D.: Offshore wind fields in near-real-time, Technical University of Denmark [data set], https://science.globalwindatlas.info/#/map, 2022.

Charnock, H.: Wind stress on a water surface, Quarterly Journal of the Royal Meteorological Society, 81, 639–640, https://doi.org/10.1002/qj.49708135027, 1955.

Chen, X.: How Do Planetary Boundary Layer Schemes Perform in Hurricane Conditions: A Comparison With Large-Eddy Simulations,
440   Journal of Advances in Modeling Earth Systems, 14, e2022MS003 088, https://doi.org/10.1029/2022MS003088, 2022.

Chen, Y., Wu, D., Li, H., and Gao, W.: Quantifying the fatigue life of wind turbines in cyclone-prone regions, Applied Mathematical Modelling, 110, 455–474, https://doi.org/10.1016/j.apm.2022.06.001, 2022.

Chu, J.-H., Sampson, R. C., Levine, S. A., and Fukada, E.: The Joint Typhoon Warning Center Tropical Cyclone Best-Tracks, 1945-2000, Tech. Rep. NRL/MR/7540-02-16, Naval Research Laboratory and Joint Typhoon Warning Center, https://www.metoc.navy.mil/
445   jtwc/products/best-tracks/tc-bt-report.html, 2002.

Dimitrov, N. K., Natarajan, A., and Kelly, M. C.: Model of wind shear conditional on turbulence and its impact on wind turbine loads, Wind Energy, 18, 1917–1931, https://doi.org/10.1002/we.1797, 2015.

Donelan, M. A., Haus, B. K., Reul, N., Plant, W. J., Stiassnie, M., Graber, H. C., Brown, O. B., and Saltzman, E. S.: On the limiting aerodynamic roughness of the ocean in very strong winds, Geophysical Research Letters, 31, L18 306 1–5,
450   https://doi.org/10.1029/2004GL019460, 2004.

Donlon, C. J., Martin, M., Stark, J., Roberts-Jones, J., Fiedler, E., and Wimmer, W.: The Operational Sea Surface Temperature and Sea Ice Analysis (OSTIA) system, Remote Sensing of Environment, 116, 140–158, https://doi.org/10.1016/j.rse.2010.10.017, 2012.

Draxl, C., Hahmann, A. N., Pena Diaz, A., and Giebel, G.: Evaluating winds and vertical wind shear from Weather Research and Forecasting model forecasts using seven planetary boundary layer schemes, Wind Energy, 17, 39–55, https://doi.org/10.1002/we.1555, 2014.

455   Dvorak, V.: Tropical cyclone intensity analysis using satellite data, Tech. Rep. NOAA technical report NESDIS ; 11, National Oceanic and Atmospheric Administration, National Environmental Satellite, Data and Information Service, United States, https://repository.library.noaa.gov/view/noaa/19322, 1984.

Emanuel, K.: An air sea interaction theory for tropical cyclones. Part 1: Steady-state maintenance, Journal of the Atmospheric Sciences, 43, 585–604, https://doi.org/doi.org/10.1175/1520-0469(1986)043<0585:AASITF>2.0.CO;2, 1986.

460   Fitch, A. C., Olson, J. B., Lundquist, J. K., Dudhia, J., Gupta, A. K., Michalakes, J., and Barstad, I.: Local and mesoscale impacts of wind farms as parameterized in a mesoscale NWP model, Monthly Weather Review, 140, 3017–3038, https://doi.org/10.1175/MWR-D-11-00352.1, 2012.

Gage, K. S. and Nastrom, G. D.: Theoretical interpretation of atmospheric wavenumber spectra of wind and temperature observed by commercial aircraft during GASP, Journal of the Atmospheric Sciences, 43, 729–40, https://doi.org/https://doi.org/10.1175/1520-
465   0469(1986)043<0729:TIOAWS>2.0.CO;2, 1986.

Garratt, J.: Review: the atmospheric boundary layer, Earth-Science Reviews, 37, 89–134, https://doi.org/https://doi.org/10.1016/0012-8252(94)90026-4, 1994.

Gopalakrishnan, S. G., Marks, F., Zhang, J. A., Zhang, X., Bao, J. W., and Tallapragada, V.: A study of the impacts of vertical diffusion on the structure and intensity of the tropical cyclones using the high-resolution HWRF system, Journal of the Atmospheric Sciences, 70, 524–541, https://doi.org/10.1175/JAS-D-11-0340.1, 2013.

Green, B. W. and Zhang, F.: Impacts of air-sea flux parameterizations on the intensity and structure of tropical cyclones, Monthly Weather Review, 141, 2308–2324, https://doi.org/10.1175/MWR-D-12-00274.1, 2013.

Harper, B. A., Kepert, J. D., and Ginger, J. D.: Guidelines for converting between various wind averaging periods in tropical cyclone conditions, Tech. Rep. WMO/TD-No. 1555, World Meteorological Organization, 2010.

He, J. Y., Chan, P. W., Li, Q. S., Li, L., Zhang, L., and Yang, H. L.: Observations of wind and turbulence structures of Super Typhoons Hato and Mangkhut over land from a 356 m high meteorological tower, Atmospheric Research, 265, https://doi.org/10.1016/j.atmosres.2021.105910, 2022.

He, Y. C., Chan, P. W., and Li, Q. S.: Observations of vertical wind profiles of tropical cyclones at coastal areas, Journal of Wind Engineering and Industrial Aerodynamics, 152, 1–14, https://doi.org/10.1016/j.jweia.2016.01.009, 2016.

Hersbach, H., Bell, B., Berrisford, P., Biavati, G., Horányi, A., Muñoz Sabater, J., Nicolas, J., Peubey, C., Radu, R., Rozum, I., Schepers, D., Simmons, A., Soci, C., Dee, D., and Thépaut, J.-N.: ERA5 hourly data on pressure levels from 1979 to present, Copernicus Climate Change Service (C3S) Climate Data Store (CDS), https://doi.org/10.24381/cds.bd0915c6, 2018.

Hong, S.-Y., Noh, Y., and Dudhia, J.: A new vertical diffusion package with an explicit treatment of entrainment processes, Monthly weather review, 134, 2318–2341, https://doi.org/https://doi.org/10.1175/MWR3199.1, 2006.

Iacono, M. J., Delamere, J. S., Mlawer, E. J., Shephard, M. W., Clough, S. A., and Collins, W. D.: Radiative forcing by long-lived greenhouse gases: Calculations with the AER radiative transfer models, Journal of Geophysical Research: Atmospheres, 113, https://doi.org/10.1029/2008JD009944, 2008.

IEC: IEC 61400-1 Ed4: Wind turbines - Part 1: Design requirements, standard, International Electrotechnical Commission, Geneva, Switzerland, 2019.

Jackson, C. R., Ruff, T. W., Knaff, J. A., Mouche, A., and Sampson, C. R.: Chasing cyclones from space, EOS, https://doi.org/10.1029/2021EO159148, 2021.

Janić, Z. I.: Nonsingular implementation of the Mellor-Yamada level 2.5 scheme in the NCEP Meso model, Tech. Rep. Office note; 437, National Centers for Environmental Prediction (United States), https://repository.library.noaa.gov/view/noaa/11409, 2001.

Jiménez, P. A., Dudhia, J., González-Rouco, J. F., Navarro, J., Montávez, J. P., and García-Bustamante, E.: A revised scheme for the WRF surface layer formulation, Monthly weather review, 140, 898–918, 2012.

Kain, J. S.: The Kain–Fritsch Convective Parameterization: An Update, Journal of Applied Meteorology, 43, 170–181, https://doi.org/https://doi.org/10.1175/1520-0450(2004)043<0170:TKCPAU>2.0.CO;2, 2004.

Kapoor, A., Ouakka, S., Arwade, S. R., Lundquist, J. K., Lackner, M. A., Myers, A. T., Worsnop, R. P., and Bryan, G. H.: Hurricane eyewall winds and structural response of wind turbines, Wind Energy Science, 5, 89–104, https://doi.org/10.5194/wes-5-89-2020, 2020.

Karagali, I., Larsén, X. G., Badger, M., Peña, A., and Hasager, C. B.: Spectral Properties of ENVISAT ASAR and QuikSCAT Surface Winds in the North Sea, Remote Sensing, 5, 6096–6115, https://doi.org/10.3390/rs5116096, 2013.

Kepert, J. D.: Choosing a boundary layer parameterization for tropical cyclone modeling, Monthly Weather Review, 140, 1427–1445, https://doi.org/10.1175/MWR-D-11-00217.1, 2012.

Krogsæter, O. and Reuder, J.: Validation of boundary layer parameterization schemes in the weather research and forecasting model
  under the aspect of offshore wind energy applications- part I: Average wind speed and wind shear, Wind Energy, 18, 769–782,
  https://doi.org/10.1002/we.1727, 2014.

Larsén, X. G., Ott, S., Badger, J., Hahmann, A. N., and Mann, J.: Recipes for correcting the impact of effective mesoscale resolution on the
  estimation of extreme winds, Journal of Applied Meteorology and Climatology, 51, 521–533, https://doi.org/10.1175/JAMC-D-11-090.1,
  2012.

Larsén, X. G., Larsen, S. E., and Lundtang Petersen, E.: Full-Scale Spectrum of Boundary-Layer Winds, Boundary-layer Meteorology, 159,
  349–371, https://doi.org/10.1007/s10546-016-0129-x, 2016.

Li, J., Li, Z., Jiang, Y., and Tang, Y.: Typhoon Resistance Analysis of Offshore Wind Turbines: A Review, Atmosphere, 13, 451,
  https://doi.org/10.3390/atmos13030451, 2022.

Ming, J., Liu, R., Zhang, J. A., and Rogers, R. F.: The Shear-Relative Variation of Inflow Angle and Its Relationship to Tropical Cyclone
  Intensification, Journal of Geophysical Research: Atmospheres, 127, e2022JD037 280, https://doi.org/10.1029/2022JD037280, 2022.

Nakanishi, M. and Niino, H.: Development of an improved turbulence closure model for the atmospheric boundary layer, Journal of the
  Meteorological Society of Japan. Ser. II, 87, 895–912, https://doi.org/10.2151/jmsj.87.895, 2009.

Nolan, D. S., Zhang, J. A., and Stern, D. P.: Evaluation of planetary boundary layer parameterizations in tropical cyclones by comparison of
  in situ observations and high-resolution simulations of Hurricane Isabel (2003). Part I: Initialization, maximum winds, and the outer-core
  boundary layer, Monthly Weather Review, 137, 3651–3674, https://doi.org/10.1175/2009MWR2785.1, 2009.

Ott, S.: Extreme winds in the Western North Pacific, Tech. Rep. No. 1544, Technical University of Denmark, 2006.

Powell, M. D., Vickery, P. J., and Reinhold, T. A.: Reduced drag coefficient for high wind speeds in tropical cyclones, Nature, 422, 279–283,
  https://doi.org/10.1038/nature01481, 2003.

Rai, D. and Pattnaik, S.: Sensitivity of Tropical Cyclone Intensity and Structure to Planetary Boundary Layer Parameterization, Asia-pacific
  Journal of Atmospheric Sciences, 54, 473–488, https://doi.org/10.1007/s13143-018-0053-8, 2018.

Rajeswari, J. R., Srinivas, C. V., Mohan, P. R., and Venkatraman, B.: Impact of Boundary Layer Physics on Tropical Cyclone Simulations in
  the Bay of Bengal Using the WRF Model, Pure and Applied Geophysics, 177, 5523–5550, https://doi.org/10.1007/s00024-020-02572-3,
  2020.

RSMC: Annual Report on the Activities of the RSMC Tokyo - Typhoon Center 2021, Tech. rep., Japan Meteorological Agency (JMA),
  https://www.jma.go.jp/jma/jma-eng/jma-center/rsmc-hp-pub-eg/AnnualReport/2021/Text/Text2021.pdf, 2021.

Shenoy, M., Raju, P. V., and Prasad, J.: Optimization of physical schemes in WRF model on cyclone simulations over Bay of Bengal using
  one-way ANOVA and Tukey's test, Scientific Reports, 11, 24 412, https://doi.org/10.1038/s41598-021-02723-z, 2021.

Skamarock, W. C.: Evaluating mesoscale NWP models using kinetic energy spectra, Monthly Weather Review, 132, 3019–3032,
  https://doi.org/10.1175/MWR2830.1, 2004.

Skamarock, W. C., Klemp, J. B., Dudhia, J., Gill, D. O., Liu, Z., Berner, J., Wang, W., Powers, J. P., Duda, M. G., Barker, D., and Huang,
  X.-Y.: A Description of the Advanced Research WRF Model Version 4.3, National Center for Atmospheric Research: Boulder, CO, USA,
  No. NCAR/TN-556+STR, 148, https://doi.org/10.5065/1dfh-6p97, 2021.

Sparks, N., Hon, K. K., Chan, P. W., Wang, S., Chan, J. C., Lee, T. C., and Toumi, R.: Aircraft observations of tropical cyclone boundary layer
  turbulence over the South China Sea, Journal of the Atmospheric Sciences, 76, 3773–3783, https://doi.org/10.1175/JAS-D-19-0128.1,
  2019.

Thompson, G., Field, P. R., Rasmussen, R. M., and Hall, W. D.: Explicit forecasts of winter precipitation using an improved bulk microphysics scheme. Part II: Implementation of a new snow parameterization, Monthly Weather Review, 136, 5095–5115, https://doi.org/0.1175/2008MWR2387.1, 2008.

Tse, K. T., Li, S. W., Chan, P. W., Mok, H. Y., and Weerasuriya, A. U.: Wind profile observations in tropical cyclone events using wind-profilers and doppler SODARs, Journal of Wind Engineering and Industrial Aerodynamics, 115, 93–103, https://doi.org/10.1016/j.jweia.2013.01.003, 2013.

Vickery, P. J., Wadhera, D., Powell, M. D., and Chen, Y.: A hurricane boundary layer and wind field model for use in engineering applications, Journal of Applied Meteorology and Climatology, 48, 381–405, https://doi.org/10.1175/2008JAMC1841.1, 2009.

Volker, P. H. J., Badger, J., Hahmann, A. N., and Ott, S.: The Explicit Wake Parametrisation V1.0: a wind farm parametrisation in the mesoscale model WRF, Geoscientific Model Development Discussions, 8, 3481–3522, https://doi.org/10.5194/gmdd-8-3481-2015, 2015.

Wang, H., Ke, S. T., Wang, T. G., Kareem, A., Hu, L., and Ge, Y. J.: Multi-stage typhoon-induced wind effects on offshore wind turbines using a data-driven wind speed field model, Renewable Energy, 188, 765–777, https://doi.org/10.1016/j.renene.2022.02.072, 2022.

Worsnop, R. P., Lundquist, J. K., Bryan, G. H., Damiani, R., and Musial, W.: Gusts and shear within hurricane eyewalls can exceed offshore wind turbine design standards, Geophysical Research Letters, 44, 6413–6420, https://doi.org/10.1002/2017GL073537, 2017.

Yang, H., Wu, L., and Xie, T.: Comparisons of four methods for tropical cyclone center detection in a high-resolution simulation, Journal of the Meteorological Society of Japan, 98, 379–393, https://doi.org/10.2151/jmsj.2020-020, 2020.

Zhang, J. A., Rogers, R. F., Nolan, D. S., and Marks, F. D.: On the characteristic height scales of the hurricane boundary layer, Monthly Weather Review, 139, 2523–2535, https://doi.org/10.1175/MWR-D-10-05017.1, 2011.

Zhang, J. A., Kalina, E. A., Biswas, M. K., Rogers, R. F., Zhu, P., and Marks, F. D.: A review and evaluation of planetary boundary layer parameterizations in hurricane weather research and forecasting model using idealized simulations and observations, Atmosphere, 11, 1091, https://doi.org/10.3390/atmos11101091, 2020.